A method for the time-frequency analysis of high-order interactions in non-stationary physiological networks

Journal of Neural Engineering

OPEN ACCESS

RECEIVED
2 April 2025

REVISED
26 September 2025

ACCEPTED FOR PUBLICATION
21 October 2025

PUBLISHED
7 November 2025

PAPER

A method for the time-frequency analysis of high-order interactions in non-stationary physiological networks

Yuri Antonacci[1], **Chiara Bará**[1], **Laura Sparacino**[1], **Gorana Mijatovic**[2], **Ludovico Minati**[3,4,5] and **Luca Faes**[1,2,*]

[1] Department of Engineering, University of Palermo, Palermo, Italy
[2] Faculty of Technical Sciences, University of Novi Sad, Novi Sad, Serbia
[3] School of Life Science and Technology, University of Electronic Science and Technology of China, Chengdu, People's Republic of China
[4] Center for Mind/Brain Sciences (CIMeC), University of Trento, Trento, Italy
[5] Nano Sensing Research Unit, Institute of Innovative Research, Institute of Science Tokyo, Yokohama, Japan
[*] Author to whom any correspondence should be addressed.

E-mail: luca.faes@unipa.it and yuri.antonacci@unipa.it

Keywords: high-order interactions, information dynamics, network neuroscience, redundancy and synergy, multivariate time series analysis, time-varying autoregressive models

Abstract

Objective. Several data-driven approaches based on information theory have been proposed for analyzing high-order interactions (HOIs) involving three or more components of a network system. The existing methods do not account for temporal correlations in the data, or are defined only in the time domain and rely on the assumption of stationarity in the underlying dynamics, making them inherently unable to detect frequency-specific behaviors and track transient functional links in physiological networks. *Approach*. This study introduces a new framework which enables the time-varying and time-frequency analysis of HOIs in networks of random processes through the spectral representation of vector autoregressive models. The time- and frequency-resolved analysis of synergistic and redundant interactions among groups of processes is ensured by a robust identification procedure based on a recursive least squares estimator with a forgetting factor. *Main results*. Validation on simulated networks illustrates how the time-frequency analysis is able to highlight transient synergistic behaviors emerging in specific frequency bands which cannot be detected by time-domain stationary analyzes. The application on brain evoked potentials in rats elicits the presence of redundant information timed with whisker stimulation and mostly occurring in the contralateral hemisphere. The application to cardiovascular oscillations reveals a reduction in redundant information following head-up tilt, reflecting a functional disconnection within the physiological network of heart period, respiratory, and arterial pressure signals. *Significance*. The proposed framework enables a comprehensive time-varying and time-frequency analysis of the hierarchical organization of dynamic networks. As our approach goes beyond pairwise interactions, it is well suited for the study of transient high-order behaviors arising during state transitions in many network systems commonly studied in physiology, neuroscience and other fields.

1. Introduction

Network models represented as graphs are essential tools for exploring the structure and dynamics of various physiological systems and their interactions [1]. In these models, each entity, such as a brain unit or an organ system, is represented as a node, while the edges map functional dependencies like brain connectivity [2] or cardiovascular interactions [3]. Although widely recognized and applied as a standard tool for many complex physiological systems, graph-based networks are limited by the underlying assumption that interactions between nodes are strictly pairwise. However, increasing evidence in neuroscience

and physiology underscores the importance of group interactions, which go beyond pairwise connections to involve the collective dynamics of groups of nodes [4]. These interactions are characterized by non-factorizability, meaning that the joint behavior of multiple components cannot be expressed as the sum of individual or pairwise contributions [4–6]. Several studies have demonstrated the presence of such non-factorizable interactions, denoted as high-order interactions (HOIs), in physiological systems. For example, HOIs have been identified in cardiovascular and respiratory networks, whose joint dynamics are modulated collectively by multiple coexisting physiological mechanisms [7–10], or in brain networks, where the complex interplay among three or more brain regions has been shown to be crucial for neural processing and behavior [5, 11–16].

Despite their importance, identifying HOIs in physiological systems remains a significant challenge, because in these systems interactions are not inherently defined but need to be inferred from data [4]. To tackle this issue, various information-theoretic metrics have been proposed, which assess the statistical concepts of synergy and redundancy among groups of random variables or processes [5, 7, 9, 17–20]. Synergy reflects statistical interactions that uniquely arise from the collective behavior of a network, meaning they cannot be deduced by examining individual components or smaller subsets in isolation; in contrast, redundancy refers to overlapping contributions, where shared information among subgroups of variables sufficiently explains the observed interactions. Interaction information [21] (II) was one of the first measures proposed to detect the balance between synergy and redundancy. More recently, this concept has been extended through the O-information [20] (OI), which provides a framework to distinguish synergy-dominated from redundancy-dominated interactions in networks of multiple interacting variables. Furthermore, given that physiological networks display temporally correlated activities, dynamic approaches measuring information rates — such as the II rate [5, 7] and the OI rate [8, 12] — have been introduced to replace traditional static quantities. These important developments opened the way to the analysis of HOIs in physiological systems represented as networks of random processes.

One of the major challenges in studying dynamic network systems is the prevalence of non-stationary behaviors [22–25]. In particular, the output dynamics of physiological systems transiently change over time with different physiological states, pathological conditions, or external stimuli [26], directly affecting pairwise and higher-order behaviors. Nevertheless, there is a substantial lack of time-varying methods capable of tracking HOIs in non-stationary settings. Moreover, since physiological systems typically exhibit oscillatory behaviors deployed across distinct frequency bands [8], the development of spectral approaches is also envisaged. In fact, while recent studies investigated the presence of HOIs in time series data in a time-resolved fashion [27, 28], these approaches rely on the local OI framework that assumes stationarity of the underlying process and does not account for temporal correlations, thus preventing time-varying and spectral analyzes.

To fill the gaps presented above, the present study introduces an approach for analyzing redundant and synergistic HOIs in multivariate stochastic processes, capturing their time-varying and time-frequency dynamics. The approach leverages methodological frameworks recently introduced to characterize the time-varying information content of individual processes [25] and the spectral content of HOIs [7, 8] to quantify redundant and synergistic interactions in non-stationary multivariate processes with coupled oscillatory components. This is achieved using linear time-varying vector autoregressive (VAR) models [29], whose frequency domain representation is exploited to assess HOIs at each time step. Model identification is performed through the recursive least squares (RLS) algorithm, which allows to map the information content of brain signals [24, 25] and their interactions in multi-trial settings and even when only a single realization of the process is available [30–36]. As a result of these developments, the existing framework for the computation of the OI rate [7] is significantly expanded through the time-frequency representation of vector random processes, the time-varying computation of full and restricted model variances, and the explicit extension to the case of multiple realizations (trials) of the underlying process. These expansions, which are not covered by the univariate single-trial modeling approach presented in [25] to study time-varying information dynamics, offer unprecedented possibilities to detect and track transient oscillatory high-order behaviors from neurophysiological data.

The proposed framework is first illustrated through theoretical examples of simulated VAR processes featuring time-variant HOIs of different types and orders across various frequency bands. It is then applied to analyze evoked potentials in electroencephalographic (EEG) signals recorded from rats during whisker stimulation [35], as well as to a physiological network comprising heart period, respiratory, and arterial pressure time series measured in the transition from rest to postural stress, where HOIs are expected to play a crucial role in shaping collective dynamics.

2. Methods

2.1. Time-resolved O-Information rate

Let us consider a set of M signals as a realization of the multivariate (vector) stochastic process $Y = \{Y_1, \ldots, Y_M\}$. Let us also denote as $Y(t_n) = [Y_1(t_n), \ldots, Y_M(t_n)]^\top \in \mathbb{R}^{M\times 1}$ the vector random variable that samples the process at the temporal index $n \in \mathbb{N}$ ($t_n = n\Delta t$, $\Delta t = 1/f_s$, f_s sampling frequency). Then, considering a generic subset $X \subseteq Y$ containing $N \leqslant M$ processes, $X = \{X_1, \ldots, X_N\} = \{Y_{i_1}, \ldots, Y_{i_N}\}$, $i_k \in \{1, \ldots, M\}$, $k = 1, \ldots, N$, the average rate of information produced at the time t_n by X is measured through its *entropy rate* (ER) [37]:

$$H_X(t_n) = H(X(t_n)\,|X^q(t_n))\,, \tag{1}$$

where $X(t_n) \in \mathbb{R}^{N\times 1}$ is the variable sampling X at the present time t_n, $X^q(t_n) = [X(t_{n-1}), \ldots, X(t_{n-q})]^\top \in \mathbb{R}^{qN\times 1}$ collects the variables sampling X over q past lags (in theory, $q \to \infty$), and $H(\cdot|\cdot)$ denotes conditional entropy [38]. The ER (1) measures the complexity of the process X at a specific time point, capturing the amount of information contained in the present time of X that cannot be explained by its past history. This measures ranges from $H_X(t_n) = 0$ for a fully self-predictable process to $H_X(t_n) = H(X(t_n))$ for a fully unpredictable process [9, 12].

Starting from the time-specific ER (1), we formulate a time-specific HOI measure which generalizes to non-stationary random processes the so-called O-information rate (OIR) defined in [7, 8]. Specifically, the time-resolved OIR of the vector process $X = \{X_1, \ldots, X_N\}$ is defined as:

$$\Omega_X(t_n) = (N-2)\,H_X(t_n) + \sum_{j=1}^{N}\left[H_{X_j}(t_n) - H_{X^j}(t_n)\right], \tag{2}$$

where $X^j = X \setminus X_j$ is the vector process obtained removing X_j from X. Note that for stationary random processes the time-resolved OIR is the same at each time step t_n, $\Omega_X(t_n) = \Omega_X$, returning the time-invariant OIR measure [7]. Equation (2) provides a null value when $N = 2$ processes are analyzed, while in the case $N = 3$ it yields a time-resolved extension of the well-known II rate [5, 7, 21]. Crucially, the time-specific OIR can be positive or negative, with the sign reflecting the redundant or synergistic nature of the analyzed group of processes. Specifically, $\Omega_X(t_n)$ takes positive values when redundant interactions dominate over synergistic ones and negative values when the opposite occurs.

2.2. Computation for linear multivariate processes

Under the assumption that the variables sampling the original vector process at each time t_n have a joint Gaussian distribution, the time-specific OIR (2) can be computed in the framework of VAR modeling [39]. Specifically, the current state of the overall process Y can be represented by a linear combination of the past states by means of a linear time-varying VAR (TV-VAR) model [29]:

$$Y(t_n) = \sum_{k=1}^{p} \mathbf{A}_k(t_n)\,Y(t_{n-k}) + U(t_n)\,, \tag{3}$$

where $\mathbf{A}_k(t_n) \in \mathbb{R}^{M\times M}$ is the time-dependent matrix of the model coefficients and $U(t_n) = [U_1(t_n), \ldots, U_M(t_n)]^\top \in \mathbb{R}^{M\times 1}$ is a vector of zero-mean innovation variables with $M \times M$ covariance matrix $\mathbf{\Sigma}_U(t_n) = \mathbb{E}[U(t_n)U(t_n)^\top]$. Then, to describe the dynamics relevant to a generic Q-dimensional sub-process $S \subseteq X$, $S \in \mathbb{R}^{Q\times 1}$, we exploit a restricted TV-VAR model:

$$S(t_n) = \sum_{k=1}^{q} \mathbf{B}_k(t_n)\,S(t_{n-k}) + U_S(t_n)\,, \tag{4}$$

where $\mathbf{\Sigma}_{U_S}(t_n) \in \mathbb{R}^{Q\times Q}$ is the covariance matrix of the innovation process feeding the restricted model and $\mathbf{B}_k(t_n) \in \mathbb{R}^{Q\times Q}$ is the relevant time-dependent coefficient matrix; note that the order q of the restricted model will theoretically tend to infinity because a sub-process of a VAR process will have a moving average component [40]. The time-specific ER of the sub-process S can be then derived from the generalized variance of the residuals in the restricted model (4), as [8]:

$$H_S(t_n) = \frac{1}{2}\log(2\pi e)^Q\,|\mathbf{\Sigma}_{U_S}(t_n)\,|, \tag{5}$$

where $|\cdot|$ stands for matrix determinant. Thus, by applying (5) $2N+1$ times, each with S taking the role of one of the processes appearing in (2), yields to compute the time-specific OIR for the set of processes collected in X.

The parameters of the full model (3), i.e. $\mathbf{A}_k(t_n)$ and $\mathbf{\Sigma}_U(t_n)$, are estimated with the TV-VAR identification procedure described in section 2.4. Then, the parameters of each restricted model (4), i.e. $\mathbf{B}_k(t_n)$ and $\mathbf{\Sigma}_{U_S}(t_n)$, are derived from those of the full model through a two-step procedure which (i) derives the time-lagged covariance structure of the full process at each time step $Y(t_n)$ by solving the Yule–Walker (YW) equations at the relevant time-step, and (ii) reorganizes such structure to relate it to the covariance of the sub-process S; a detailed description of the practical solution of the YW equations can be found in [10, 24]. The order p of the full model is estimated as described in section 2.4, while the order q of the restricted models is set at a high value to capture the decay of the correlation function [41].

2.3. Time–frequency expansion

The time–frequency analysis of HOIs can be implemented exploiting the spectral representation of VAR models [42] and observing that the TV-VAR model (3) admits a stationary representation at each time step t_n [43]. This representation provides the transfer matrix relating the Fourier transform (FT) of the processes U and Y in (3), obtained at each time instant t_n as the inverse of the FT of the time-specific model coefficients through the relation [30, 42, 44]

$$\mathbf{H}(t_n,\omega) = \left[\mathbf{I} - \sum_{k=1}^{p} \mathbf{A}_k(t_n)\, \mathrm{e}^{-\mathbf{j}\omega k}\right]^{-1}, \qquad (6)$$

where $\omega \in [-\pi,\pi]$ is the normalized angular frequency ($\omega = 2\pi \frac{f}{f_s}$ with $f \in \left[-\frac{f_s}{2},\frac{f_s}{2}\right]$), $\mathbf{j} = \sqrt{-1}$, and $\mathbf{I}$ is the $M \times M$ identity matrix.

Starting from (6), the power spectral density (PSD) of the overall process relevant to the time-step t_n can be expressed as $\mathbf{P}_Y(t_n,\omega) = \mathbf{H}(t_n,\omega)\mathbf{\Sigma}_U(t_n)\mathbf{H}^*(t_n,\omega)$ [42], where * stands for conjugate transpose. Then, the PSD matrix of Y can be pruned to extract the PSD of any generic sub-process S satisfying (4), $\mathbf{P}_S(t_n,\omega)$. Based on this partition, the spectral ER of the sub-process S is defined as [5, 8]

$$h_S(t_n,\omega) = \frac{1}{2}\log\left(2\pi e\right)^Q |\mathbf{P}_S(t_n,\omega)|, \qquad (7)$$

yielding a time-frequency measure of the complexity of the process S. Importantly, the spectral and time domain definitions of ER given in (7) and (5) are closely related to each other by the spectral integration property [45], in a way such that the integration of the spectral ER over the whole frequency axis returns the time-specific ER (5) [8]:

$$H_S(t_n) = \frac{1}{2\pi}\int_{-\pi}^{\pi} h_S(t_n,\omega)\,\mathrm{d}\omega. \qquad (8)$$

Given (8) and (2), it is easy to show that a spectral version of the time-specific OIR of the N processes in X is given by:

$$\nu_X(t_n,\omega) = (N-2)\, h_X(t_n,\omega) + \sum_{j=1}^{N}\left[h_{X_j}(t_n,\omega) - h_{X^j}(t_n,\omega)\right], \qquad (9)$$

which, in turn, satisfies the spectral integration property, i.e. $\Omega_X(t_n) = \frac{1}{2\pi}\int_{-\pi}^{\pi}\nu_X(t_n,\omega)\mathrm{d}\omega$. Therefore, the spectral version of the time-resolved HOI measure (2) defined in (9) can be meaningfully interpreted as a time- and frequency-specific index of the synergistic/redundant information shared by multiple stochastic processes.

2.4. Model identification

Here we describe the procedure followed for the practical computation of the time-frequency OIR measure, which is based on the RLS estimation of the TV-VAR model (3) [24, 30]. The procedure starts with R realizations of the analyzed vector process Y, available in the form of R multivariate time series each composed by M series measured over T samples: $y^{(r)}(t_i) \in \mathbb{R}^{M\times 1}, r = 1,\ldots,R, i = 1,\ldots,T$. From this dataset, the following observation matrices are formed for each time step t_n, $n = p+1,\ldots,T$: $\mathbf{Y}(t_n) = [y^{(1)}(t_n),\ldots,y^{(R)}(t_n)] \in \mathbb{R}^{M\times R}$, containing the observations of the present state of Y; $\mathbf{W}(t_n) = [w^{(1)}(t_n),\ldots,w^{(R)}(t_n)] \in \mathbb{R}^{Mp\times R}$, with $w^{(r)}(t_n) = [y^{(r)}(t_{n-1})^\top,\ldots,y^{(r)}(t_{n-p})^\top]^\top \in \mathbb{R}^{Mp\times 1}$, containing the observations of the p past states of Y. With this notation, a compact representation of the time-varying model (3) can be obtained as: $\mathbf{Y}(t_n) = \mathbf{A}(t_n)\mathbf{W}(t_n) + \mathbf{U}(t_n)$, where $\mathbf{A}(t_n) = [\mathbf{A}_1(t_n),\ldots,\mathbf{A}_p(t_n)] \in \mathbb{R}^{M\times Mp}$ is the matrix of unknown VAR coefficients at time t_n while $\mathbf{U}(t_n) = [u^{(1)}(t_n),\ldots,u^{(R)}(t_n)] \in \mathbb{R}^{M\times R}$, with $u^{(r)}(t_n) \in \mathbb{R}^{M\times 1}$, contains the observations of the innovation process U.

The RLS involves the minimization of a cost function defined as [24, 29]: $\mathcal{E}(\mathbf{Y},\hat{\mathbf{Y}}) = \sum_{n=p+1}^{T}(1-c)^{T-n}||\mathbf{Z}(t_n)||^2$, where the matrix $\mathbf{Z}(t_n) = \mathbf{Y}(t_n) - \hat{\mathbf{A}}(t_{n-1})\mathbf{W}(t_n) \in \mathbb{R}^{M\times R}$ denotes the *a-priori* estimation error computed as difference between the matrix of the real data $\mathbf{Y}(t_n)$ and the estimated data $\hat{\mathbf{Y}}(t_n)$. The term $(1-c)^{T-n}$ is the exponential weighting factor or forgetting factor, with $0 < (1-c) \leqslant 1$, which can be roughly interpreted as the memory of the algorithm ensuring that the data in the distant past are 'forgotten' to follow the variations of the statistical properties of Y in non-stationary conditions; this parameter controls the trade-off between the adaption speed at transition and the variance of the estimate. The RLS algorithm to estimate the matrix of VAR coefficients consists in [24, 32]: (i) choose a value for the adaptation factor c and an order of the TV-VAR model p; (ii) define proper initial conditions for the VAR coefficients at time t_p, $\mathbf{A}(t_p) = [\mathbf{A}_1(t_p),\ldots,\mathbf{A}_p(t_p)] \in \mathbb{R}^{M\times Mp}$, and for the correlation matrix of the past states of Y stored in $\mathbf{W}(t_p)$, $\mathbf{\Phi}^w(t_p) \in \mathbb{R}^{Mp\times Mp}$; (iii) for $t_n = t_{p+1}$ to t_T repeat the following steps:

$$\mathbf{\Phi}^w(t_n) = (1-c)\,\mathbf{\Phi}^w(t_{n-1}) + \mathbf{W}(t_n)\,\mathbf{W}(t_n)^\top, \qquad (10a)$$

$$\mathbf{K}(t_n) = (\mathbf{\Phi}^w(t_n))^{-1}\mathbf{W}(t_n), \qquad (10b)$$

$$\mathbf{Z}(t_n) = \mathbf{Y}(t_n) - \hat{\mathbf{A}}(t_{n-1})\mathbf{W}(t_n), \qquad (10c)$$

$$\hat{\mathbf{A}}(t_n) = \hat{\mathbf{A}}(t_{n-1}) + \mathbf{Z}(t_n)\,\mathbf{K}(t_n)^\top, \qquad (10d)$$

where $\mathbf{K}(t_n) \in \mathbb{R}^{Mp\times R}$ is the so-called gain matrix. A detailed mathematical derivation of the RLS solution is reported in the supplemental material of [24].

When $0 < c < 1$, a recursive computation of the time-varying covariance matrix of the residuals $\mathbf{\Sigma}_U(t_n)$ can be obtained as follows [46]:

$$\hat{\mathbf{\Sigma}}_U(t_n) = \hat{\mathbf{\Sigma}}_U(t_{n-1}) + c\left(\frac{\mathbf{Z}(t_n)\mathbf{Z}(t_n)^\top}{R} - \hat{\mathbf{\Sigma}}_U(t_{n-1})\right), \quad (11)$$

while when $c = 0$ (i.e. assuming stationarity for Y):

$$\hat{\mathbf{\Sigma}}_U(t_n) = \hat{\mathbf{\Sigma}}_U(t_{n-1}) + \frac{1}{t_n}\left(\frac{\mathbf{Z}(t_n)\mathbf{Z}(t_n)^\top}{R} - \hat{\mathbf{\Sigma}}_U(t_{n-1})\right). \quad (12)$$

The model order of the TV-VAR model (3) can be determined through computation of the mean squared prediction error (MSPE), $\frac{1}{T-p}\sum_{n=p+1}^{T}||\mathbf{Z}(t_n)||^2$; specifically, the optimal order is selected as the minimum MSPE averaged over the M processes after scanning for values of p between 1 and a maximum order P [45, 47]. We note that when $c = 0$ the process Y is considered as globally stationary and the RLS algorithm is applied 'with infinite memory' [29] reducing to the well-known ordinary least squares (OLS) estimator [48] applied over the whole time series of length T. On the other hand, by assuming $c = 1$ the process is interpreted as 'memory-less' and, if multiple realizations are available ($R \geqslant M^2p$ to ensure the existence of the solution [49]), the use of the OLS estimator allows a time-resolved identification; specifically, by setting $c = 1$ in (10d) the VAR coefficients are estimated at each time step $t_n \geqslant t_{p+1}$ through the well-known OLS formula: $\hat{\mathbf{A}}(t_n) = \mathbf{Y}(t_n)\mathbf{W}(t_n)^\top[\mathbf{W}(t_n)\mathbf{W}(t_n)^\top]^{-1}$ and $\hat{\mathbf{U}}(t_n) = \mathbf{Y}(t_n) - \hat{\mathbf{A}}(t_n)\mathbf{W}(t_n)$, whose covariance matrix $\hat{\mathbf{\Sigma}}_U(t_n)$ is an estimate of $\mathbf{\Sigma}_U(t_n)$.

3. Simulation study

This section presents the design and implementation of a benchmark simulation of multiple interacting stochastic processes highlighting the peculiar features of the proposed time-varying and time-frequency analysis of HOIs. Specifically, we show how different patterns of redundancy and synergy can emerge in different time windows and coexist at different frequencies, and would remain undetected if the standard stationary time-domain analysis was performed. Additionally, we examine the performance of the RLS algorithm in tracking sudden changes in HOIs, emphasizing the role of the forgetting factor and of the number of realizations available for the estimation. The MATLAB code to reproduce the simulation study, along with a detailed documentation, is available at: https://github.com/YuriAntonacci/tv-OIR-toolbox.

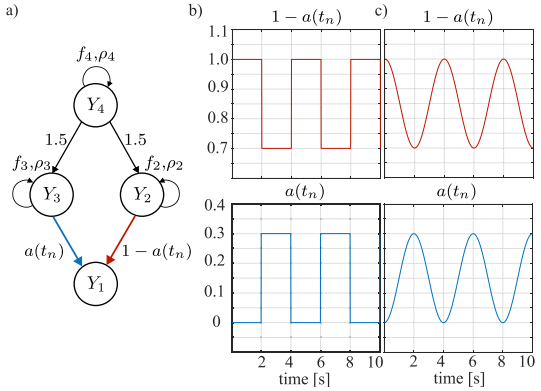

Figure 1. (a) Graphical representation of the time-varying VAR process generated according to (13), where each node represents a different scalar process and the arrows represent the imposed causal interactions (self-loops depict the influences from the past to the present sample of a process). The blue and red arrows represent time-varying coupling parameters which are modulated as depicted in (b) and (c).

3.1. Theoretical analysis

We design a four-variate time-varying VAR process with regression coefficients modulated temporally according to predefined waveforms for inducing multiple transitions within a predefined time window [5, 24]. The analyzed TV-VAR process is:

$$\begin{aligned}
Y_1(t_n) &= (1 - a(t_n))\,Y_2(t_{n-1}) + a(t_n)\,Y_3(t_{n-2}) + U_1(t_n),\\
Y_2(t_n) &= \sum_{k=1}^{2} a_{2k}Y_2(t_{n-k}) + 1.5Y_4(t_{n-1}) + U_2(t_n),\\
Y_3(t_n) &= \sum_{k=1}^{2} a_{3k}Y_3(t_{n-k}) + 1.5Y_4(t_{n-2}) + U_3(t_n),\\
Y_4(t_n) &= \sum_{k=1}^{2} a_{4k}Y_4(t_{n-k}) + U_4(t_n), \quad (13)
\end{aligned}$$

where $U_1(t_n), \ldots, U_4(t_n)$ are white and uncorrelated Gaussian processes with zero mean and unit variance. The process is simulated assuming a sampling frequency $f_s = 100$ Hz. The time-varying nature of the process is determined by the coupling parameter $a(t_n)$ modulating reciprocally the strength of the causal connections $Y_2 \to Y_1$ and $Y_3 \to Y_1$ as reported in figure 1; specifically, $a(t_n)$ is set to vary over time as a periodic square waveform, or as a periodic sinusoidal waveform, both oscillating in amplitude between 0 and 0.3 with a period of 4 s. The other simulated causal connections are $Y_4 \to Y_3$ and $Y_4 \to Y_2$, both with time-independent strength set to 1.5. Moreover, autonomous oscillations are set for the processes Y_i, $i = 2, 3, 4$, by setting time-independent coefficients $a_{i1} = 2\rho_i \cos(2\pi f_i/f_s)$ and $a_{i2} = -\rho_i^2$, with $\rho_2 = \rho_3 = \rho_4 = 0.85$ and $f_2 = f_3 = 10$ Hz and $f_4 = 35$ Hz, so as to resemble the α and β brain rhythms.

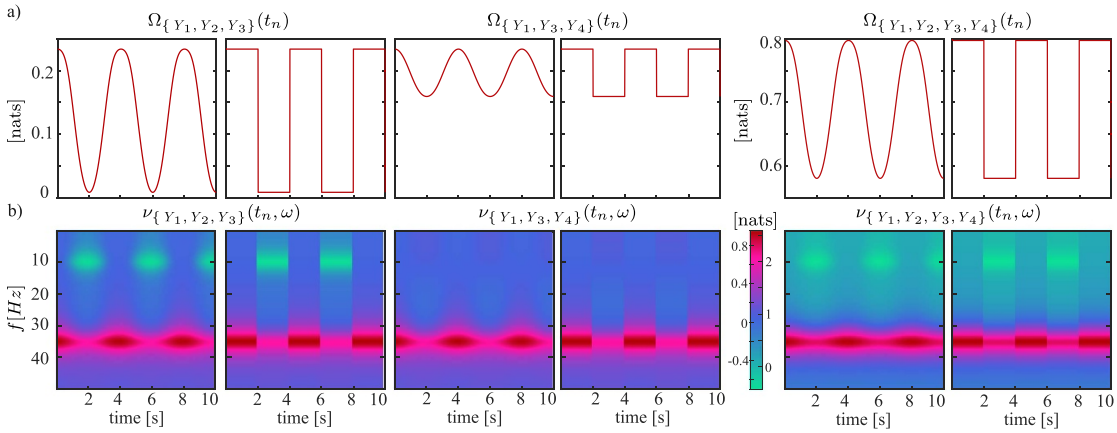

Figure 2. Time-resolved OIR and its spectral version computed for the simulated VAR process (13), driven by square and sinusoidal periodic waveforms oscillating as depicted in figure 1. (a) Time-specific OIR measure of 3rd-(i.e. $\Omega_{\{Y_1,Y_2,Y_3\}}(t_n)$, $\Omega_{\{Y_1,Y_3,Y_4\}}(t_n)$) and 4th-order (i.e. $\Omega_{\{Y_1,Y_2,Y_3,Y_4}(t_n)\}$) evidencing the presence of redundancy and multiple state transitions every 2 s. (b) Time–frequency profiles of 3rd- and 4th-order highlighting the coexistence of redundant and synergistic effects in different frequency bands.

The time–frequency representation of the TV-VAR process can be obtained by deriving its PSD directly from the true TV-VAR coefficients as described in section 2.3, from which the exact values of both the spectral and the time-specific versions of the OIR are obtained at any order of interaction. In particular, the theoretical profiles of the time-varying and time-frequency representation of the OIR are shown in figure 2 for multiplets of order three ($X = \{Y_1, Y_2, Y_3\}$ and $X = \{Y_1, Y_3, Y_4\}$) and for the full process ($X = Y$). The time-specific analysis (figure 2(a)) reveals the predominance of redundancy in the system, documented by the positive values displayed by the time-domain OIR for all the analyzed multiplets of processes. The amount of net redundancy is modulated over time according to the variable coupling from Y_3 and Y_2 to Y_1, with OIR values changing proportionally to $(1 - a(t_n))$. These results document the importance of performing a time-varying analysis in order to track the variations over time of the redundancy/synergy balance, here modulated by the strength of the chain effect $Y_4 \to Y_2 \to Y_1$ (producing redundancy) relative to that of the common child effect $Y_3 \to Y_1 \leftarrow Y_2$ (producing synergy) [5, 8]. Moreover, the time-frequency analysis of HOIs (figure 2(b)) reveals the coexistence of redundant and synergistic interactions with extent depending on the coupling parameter $a(t_n)$. Specifically, the time-frequency OIR $\nu_{\{Y_1,Y_2,Y_3\}}(t_n,\omega)$, and more smoothly also $\nu_{\{Y_1,Y_2,Y_3,Y_4\}}(t_n,\omega)$, display net redundancy in the band centered around 35 Hz when $a(t_n) \sim 0$, which becomes less pronounced and accompanied by evident net synergy around 10 Hz when $a(t_n) > 0$. These patterns document the importance of analyzing time-varying HOIs in the frequency domain to reveal effects that may remain hidden in the time domain: in our simulation the chain $Y_4 \to Y_2 \to Y_1$ and the common child $Y_3 \to Y_1 \leftarrow Y_2$, which are both active when $a(t_n)$ grows towards 0.3, yield contemporaneously synergy at ~ 10 Hz and redundancy at ~ 35 Hz, while only the chain effect producing redundancy is present in the time epochs during which $a(t_n)$ takes low values.

3.2. Practical estimation

To investigate the performance of the proposed methodology, the time-varying OIR relevant to the whole system (13), i.e. Ω_X computed with $X = \{Y_1, Y_2, Y_3, Y_4\}$, was estimated applying the procedure described in section 2.4 on realizations of the TV-VAR model of length $T = 1000$ (corresponding to a time window of 10 s). Two analyzes were performed, both varying the number of realizations generated ($R \in \{10, 20, 50, 100\}$) and the forgetting factor ($(1 - c) \in \{0, 0.5, 0.7, 0.9, 0.94, 0.96, 0.97, 0.98, 0.999\}$): the first aimed at studying the capability of the time-varying OIR estimator to follow fast and slow variations of the coupling parameter (square and sinusoidal waveforms), and the second aimed at quantifying bias and variance of the OIR estimated during the stationary phases of the periodic square variations of the coupling parameter. In both cases, the model order was estimated as described in section 2.4, q was set to 30 and the matrix $\mathbf{A}(t_p)$ was assigned drawing random samples from the uniform distribution between –1 and 1 [25]. To evaluate estimation performance, we computed the distributions of the estimated OIR values, $\hat{\Omega}_X(t_n)$, across 100 independent repetitions and compared them with the exact theoretical values derived from the true model parameters.

3.2.1. Tracking capability and transition response

Figure 3 shows the distributions of $\hat{\Omega}_X(t_n)$ across 100 iterations, computed for different values of $1 - c$ and numbers of realizations R, and compared with the

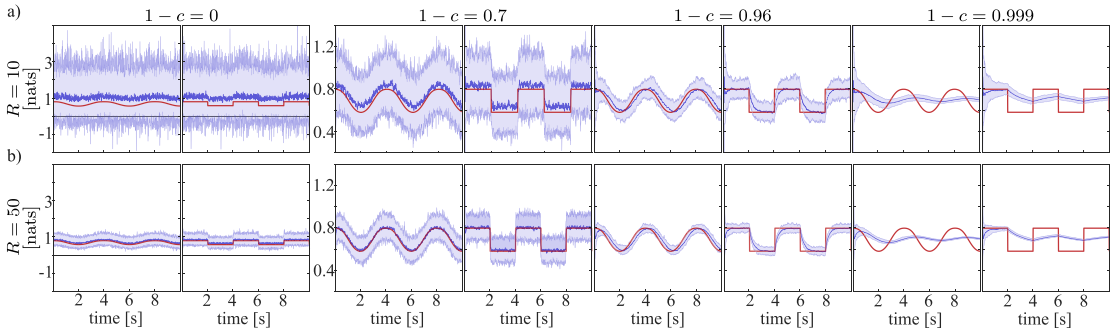

Figure 3. Distributions of the OIR $\hat{\Omega}_{\{Y_1,Y_2,Y_3,Y_4\}}(t_n)$ (median and 5th − 95th percentiles) estimated over 100 iterations of (13), for different values of $(1-c) \in \{0, 0.7, 0.96, 0.999\}$ and for different waveforms of $a(t_n)$, displayed separately after generating (a) $R = 10$ realizations or (b) $R = 50$ realizations. In each panel, the profile of the theoretical OIR $\Omega_{\{Y_1,Y_2,Y_3,Y_4\}}(t_n)$ is reported in red.

exact values derived from the true model parameters (red line). The number of realizations influences both the bias and the variance of the estimates, which are reduced substantially moving from $R = 10$ to $R = 50$. On the other hand, the forgetting factor appears to affect the bias and variance of the TV-OIR estimates in a more complex way: while the variance is always reduced at increasing of the forgetting factor, the bias is affected in a way that also depends on the waveform whereby the coupling coefficient changes. The bias generally decreases with a higher forgetting factor, but for large values, the response time to transitions also affects it — higher $(1-c)$ reduces responsiveness. This issue is more pronounced during very fast transitions (e.g. square-wave coupling coefficient).

3.2.2. Systematic analysis of bias-variance tradeoff

For each combination of the parameters $((1-c), R)$, the normalized bias was computed as $\text{BIAS}_\text{N} = \frac{1}{T}\sum_{i=1}^{T} \frac{|\Omega_X(t_i) - \hat{\Omega}_X(t_i)|}{\Omega_X(t_i)}$, and the variance was computed as $\text{VAR} = \frac{1}{T}\sum_{i=1}^{T}(\hat{\Omega}_X(t_i) - \hat{\Omega}_X^m)^2$ with $\hat{\Omega}_X^m = \frac{1}{T}\sum_{i=1}^{T}\hat{\Omega}_X(t_i)$, where $\Omega_X(t_i)$ and $\hat{\Omega}_X(t_i)$ denote the theoretical and estimated values (mean over R realizations) of the OIR at a specific time instant. After averaging $\Omega_X(t_i)$ across the 100 iterations, to quantify responsiveness, the fall time (F_t) was computed — defined as the time needed for the OIR estimate to drop from 90% to 10% of its maximum value. Then, a two-way repeated measures ANOVA was carried out separately for the performance measures BIAS_N and *VAR* to assess the effects of the factors R and $(1-c)$ on $\hat{\Omega}_X(t_n)$. The Mauchly's test of sphericity was applied, and when necessary, the Greenhouse–Geisser correction was used to adjust for violations of the sphericity assumption in all analyzes. Post-hoc comparisons between sub-levels of the ANOVA factors were conducted using Tukey's test. Results, summarized in table 1, show F-values and partial eta squared (η_p^2) for effect size, revealing a significant influence of the within-subject factors R and $(1-c)$, as well as their interaction $R \times (1-c)$, on both performance measures.

Table 1. Two-way ANOVA (degrees of freedom (DoF) and F values with effect size (η_p^2)) computed considering BIAS_N and VAR as dependent variables; **, $p < 10^{-5}$.

Factor	DoF	BIAS_N (η_p^2)	VAR (η_p^2)
R	3, 297	3355^{**} (0.971)	$16\,900^{**}$ (0.994)
$(1-c)$	9, 891	$66\,300^{**}$ (0.998)	$28\,200^{**}$ (0.996)
$R \times (1-c)$	27, 2673	$28\,000^{**}$ (0.996)	$15\,500^{**}$ (0.993)

Figure 4 shows the distributions of the performance measures as a function of the factors R and $(1-c)$. The estimation bias (BIAS_N, figure 4(a)) decreases as the number of realizations increases, with an effect that is statistically significant only when $(1-c) < 0.94$ (Tukey's post-hoc test). The estimation variance (VAR, figure 4(b)) displays a similar trend, decreasing significantly with increasing the number of realizations R when $(1-c) < 0.94$ but also when $(1-c) > 0.98$. The response time to transitions (F_t) reveals a significant impact of the number of realizations R on the RLS algorithm's ability to detect transitions for all values of the forgetting factor $(1-c) \in [0, 0.8]$; for instance, when $(1-c) = 0$ and $R \in \{10, 20\}$, the bias is so high that the fall time reaches its maximum value of 2 seconds, indicating that the transition cannot be detected.

3.2.3. Discussion and practical recommendations

Overall, the results underscore the significant influence of the number of realizations and the forgetting factor on the bias-variance trade-off and on the time required to detect transitions. Our findings align with previous studies, which have highlighted the consistency and accuracy of the RLS algorithm in estimating time-varying information-theoretic measures [24, 25], as well as coupling and causality measures [30–33]. Specifically, we find that the bias-variance trade-off is more influenced by the number of realizations than by the value of the forgetting factor. Nevertheless, the forgetting factor directly affects

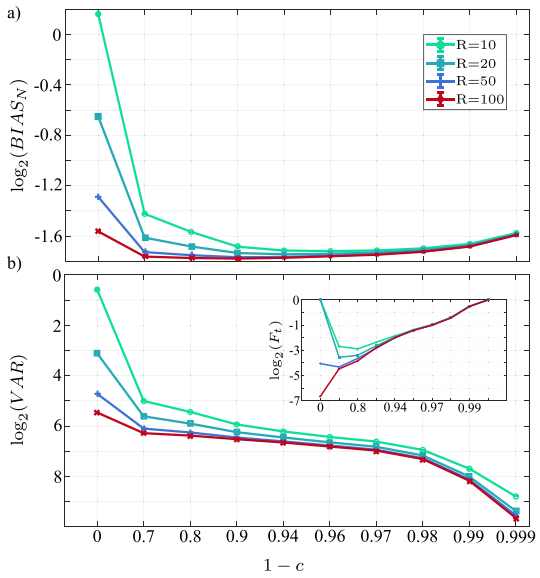

Figure 4. Performance measures (a) of bias ($BIAS_N$) and (b) variance (VAR) as a function of the factors R and $1-c$. Both measures are reported as mean value and 95% confidence interval computed across 100 iterations for each experimental condition. The inset in (b) reports the fall time computed after averaging $\hat{\Omega}_X$ across the 100 iterations.

the adaptation speed to transitions, which remains largely independent of the number of realizations, as also shown in [31]. Notably, with a sufficient number of realizations, a low forgetting factor enables precise tracking of rapid HOI transitions in dynamic systems. If this is not the case, the analysis conducted here identifies a suitable range for the forgetting factor, $0.96 \leqslant (1-c) \leqslant 0.98$, to achieve an optimal balance between bias, variance, and the ability to track abrupt transitions, as also highlighted in a previous work [24]. To provide practical recommendations we advise that, if the analysis aims to determine the time of transition in a system with minimal uncertainty when a sufficient number of realizations is available (e.g. $R > 50$), a small value for the forgetting factor is recommended. Conversely, if the number of realizations is limited (e.g. $R \leqslant 20$), a value of $(1-c)$ around 0.96–0.98 is recommended to allow proper TV-VAR identification. It is important to note that the VAR model identified at each time step t_n (when $1-c=0$) via the OLS method cannot ensure a stable solution when the number of data samples available for the estimation procedure (R in this case) is at least one order of magnitude greater than the number of VAR parameters to be estimated [49, 50].

4. Application to time-varying physiological networks

This section presents the application of the proposed framework for time- and frequency-specific analysis of HOIs to two benchmark datasets.

The first dataset includes time series of heart period, respiratory, and arterial pressure variability, used to analyze cardiovascular and cardiorespiratory interactions during orthostatic stress induced by postural changes [51]. This condition modulates the sympatho-vagal balance, leading to alterations in both cardiovascular and cardiorespiratory interactions within specific frequency bands, driven by well-characterized physiological mechanisms such as the baroreflex and respiratory sinus arrhythmia [52–54]. The time–frequency analysis is focused on the two frequency bands of physiological interest, i.e. the low-frequency (LF, 0.04–0.15 Hz) and high-frequency (HF, 0.15–0.4 Hz) bands, to illustrate how distinct physiological mechanisms operating within these bands can be described through the synergy/redundancy balance. As such, this experimental paradigm provides a controlled and well-understood model of neural autonomic regulation, suitable for benchmarking time- and frequency-resolved analyzes of physiological interactions.

The second dataset comprises epicranial EEG signals recorded during whisker stimulation in rats [55, 56]. The sensorimotor system of rodents represents a simple model of large-scale networks where the structural and functional pathways are well-known and established. In this specific context, the brain regions activated and the timing of stimulus encoding have been previously reported, together with analyzes investigating causal brain interactions and information dynamics [25, 35, 36, 56]. Here, we analyze the spatiotemporal and spectral patterns of the OIR with the aim of characterizing the extent, latency and frequency bands of the high-order mechanisms involved in brain information processing.

4.1. Cardiovascular and cardiorespiratory interactions during orthostatic stress

The analysis was performed on the time series relevant to 20 young healthy subjects (11 female; median age 19.4 yrs) selected from a database collected to study cardiovascular response to orthostatic stress [57–59]. The study protocol consisted of two consecutive phases: supine rest (REST, 15 min) and head-up tilt (HUT), where each subject was tilted to 45 degrees for 8 min to evoke mild orthostatic stress. During the entire procedure, electrocardiographic (ECG) and arterial blood pressure (BP), obtained through the volume-clamp photoplethysmographic method, were simultaneously recorded. The respiratory signal was measured through the respiratory inductance plethysmography method using both thoracic and abdominal impedance belts. From these signals, three time series were measures on a beat-to-beat basis: the nth heart period (i.e. RR_n) was computed as the time distance between the nth and the $(n+1)$th R peaks of the ECG; the nth systolic arterial pressure (SAP) value

(i.e. SAP_n) was measured as the maximum of the BP signal inside RR_n; the nth respiration amplitude (RESP) value (i.e. $RESP_n$) was computed sampling the respiration signal on the nth R peak of the ECG. For each subject, segments of $N = 1000$ points were selected synchronously for the three series; the selected windows were centered on the transition from rest to tilt (figure 5(a)). Before the analysis, the series were high-pass filtered (cut-off frequency 0.0156 Hz) and then reduced to zero mean. The resulting time series were considered as realizations of the vector stochastic process X composed by $M = 3$ scalar processes, i.e. $Y_1 = \mathrm{RR}$, $Y_2 = \mathrm{SAP}$, $Y_3 = \mathrm{RESP}$.

The analysis was performed computing the time-frequency OIR of order 3 after identifying the TV-VAR model (3) as described in sections 2.3 and 2.4 and by considering as sampling frequency (f_s) the inverse of the mean RR interval. The model order was selected via the MSPE procedure, setting the forgetting factor to $(1-c) = 0.975$ [24] and the order q of the reduced models to 30 [14], and initializing the coefficient matrix ($\mathbf{A}(t_p)$) with coefficients randomly sampled from a uniform distribution in the range $[-1, 1]$. Starting from the the time-frequency OIR $\nu_{\{Y_1,Y_2,Y_3\}}(t_n, \omega)$, time-resolved OIR was obtained through integration over the whole frequency axis or within the LF and HF range. The three profiles were averaged within each experimental phase (delimited by the dotted black line, figure 5(a)), yielding one value for REST and one for HUT for each subject.

Figures 5(b) and (c) shows the grand-average distributions of the time-varying and time-frequency OIR trends computed for the triplet $\{\mathrm{RR}, \mathrm{SAP}, \mathrm{RESP}\}$. The results reveal a redundant interaction of order 3 ($\Omega_{\{Y_1,Y_2,Y_3\}}(t_n) > 0$) during REST, followed by an abrupt decrease at the onset of the HUT condition. The time–frequency representation of OIR ($\nu_{\{Y_1,Y_2,Y_3\}}(t_n, \omega)$) further shows that redundancy during REST is primarily concentrated within the HF band. In contrast, with the transition to HUT, the net redundancy in the HF band sharply declines, while a weaker but noticeable redundant interaction emerges in the LF band, peaking near 0.1 Hz. As documented in figure 5(d), these global and frequency-specific changes induced in the OIR by the orthostatic stress are statistically significant.

The analysis confirms previous works documenting that redundancy dominates cardiovascular and cardiorespiratory interactions [52, 53, 57, 60]. Our results show that net redundancy characterizes these multivariate interactions across all frequency bands and conditions, but its extent is modulated by the transition from REST to HUT which induces a main reduction of net redundancy in the HF band and a moderate but significant increase in the LF band. We interpret the overall decrease in redundancy as a marker of network decoupling evoked by tilt and related to the known shift of the sympatho-vagal balance towards sympathetic activation and vagal

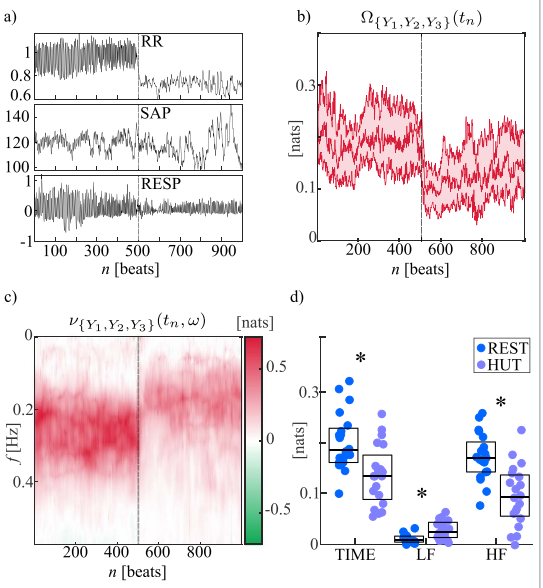

Figure 5. (a) Time series of heart period (RR[s]), systolic arterial pressure (SAP[mmHg]) and respiratory volume (RESP[L]) measured during resting supine (REST) and orthostatic stress (HUT) conditions for one representative subject. (b)–(c) Average profiles across subjects (line: median; shades: 1st–3rd quartiles) of the time-varying and time–frequency OIR of order 3. (d) Distribution (boxplots and individual values) of the mean OIR obtained integrating the time–frequency OIR measure over the whole frequency axis (TIME), in the range 0.04–0.15 Hz (LF) or in the range 0.15–0.4 Hz (HF); asterisks denote statistically significant difference between the REST and HUT conditions (Two-sided Wilcoxon signed-rank test, $p < 0.05$).

deactivation related to postural stress [61]. Indeed, the decrease of the redundancy during HUT aligns with the known reduced coupling between heart period and respiration, consistent with a diminished respiratory sinus arrhythmia mechanism resulting from parasympathetic withdrawal; this effect is localized within the HF band which typically reflects respiration-related modulations of the heart rate [42, 60, 62, 63]. On the other hand, the increased redundant interactions in the LF band during HUT likely reflect enhanced cardiovascular and cardiorespiratory interactions potentially driven by sympathetic activation. This interpretation is corroborated by the well-known tilt-induced activation of the baroreflex mechanism which determines enhanced coupling between RR and SAP in the LF band [57, 60, 63, 64] as well as the fact that slowly varying respiration patterns (mostly related to spontaneous changes of the respiratory pattern) have shown to enhance during postural stress the respiratory sinus arrhythmia along the baroreflex path RESP $\rightarrow$ SAP $\rightarrow$ RR [65].

4.2. Analysis of somatosensorial evoked responses

The analyzed dataset refers to epicranial EEG data recorded from 10 young Wistar rats according to the procedures detailed in previous works [55, 56]. Specimens were anesthetized with light isoflurane maintained at 2.5% and mounted in a stereotaxic

frame providing a continuous flow of isoflurane in the same air mixture. Epicranial signals were recorded with a custom-made amplifier from an array of 16 stainless steel electrodes 500 μm in diameter placed to cover the entire skull surface without touching head muscles (gain 5000×; band-pass filters 1–500 Hz; final impedance ∼50 kΩ). Electrode coordinates from bregma for the right and left hemispheres were (rostrocaudal/mediolateral) as follows (figure 6(a)): −7.5/4 mm (E1, E15), −4.75/5 (E2, E14), −3.5/2.25 (E3, E13), −1.5/5 (E4, E12), −0.75/2.25 (E5, E11), 1.25/4 (10E6, E10), 3.25/2.25 (E7, E9), 0/0 (E8), −6.25/0 (R), and ground electrode at 6/0 (G). All differential voltages were digitally converted at 2 kHz using custom-made scripts.

Unilateral stimuli were delivered simultaneously to all large whiskers on one side of the snout through a solenoid-based stimulator device. Large whiskers on one side of the snout were glued together and inserted in a thin tube attached to the stimulator probe that was then placed 1 cm away from the whisker pad. Each stimulus consisted of 500 μm backand-forth deflections with 1 ms rise time. Right-sided series of 50 stimuli were applied with an interstimulus interval of 9 s. The entire dataset can be found at https://doi. org/10.6084/m9.figshare.5909 122.v1.

We firstly examined the somatosensory evoked potentials (SEPs) obtained through a straightforward averaging procedure, focusing on the activity recorded at specific electrodes in response to the 50 stimuli delivered. The grand-average analysis of SEPs , illustrated in figure 6(b), reveals a voltage peak over the primary sensory cortex contralateral (cS1, electrode E12) initiating ∼ 5 ms after the onset of stimulation and vanishing 20 ∼ 30 ms later [35, 56]. Additionally, the SEP cS1 has well-defined structural connections to particular contralateral parietal, frontal sensorymotor regions (electrodes E14, E10), which become active immediately following cS1 (figure 6(b), upper panel). This is also true for the central regions (E11, E13), although the activation in these areas appears more delayed and less widespread. On the other hand, the ipsilateral S1 (iS1, electrode E4) and its neighboring electrodes (E2, E6) show involvement only at later latencies (∼ 35-50 ms after the onset), while E3 and E5 exhibit an almost complete lack of activity; as suggested in previous works [66] (figure 6(b), lower panel), although this secondary network shares the same structural and functional connections as the contralateral hemisphere, these connections are less pronounced.

To analyze the time–frequency modifications of possible high-order behaviors emerging during whisker stimulation, we considered the EEG signals recorded from ten electrodes placed in the contralateral (E10, E11, E12, E13, E14) and ipsilateral (E2, E3, E4, E5, E6) brain hemispheres. For each specimen, the signals recorded from these electrodes during repeated stimuli were interpreted

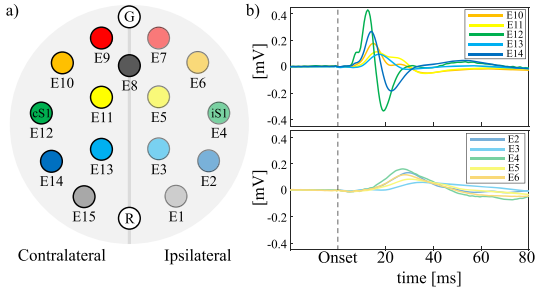

Figure 6. (a) Electrode montage for epicranial multichannel EEG. (b) Grand-average SEP for the contralateral (top) and ipsilateral (bottom) hemisphere to the right whisker stimulation.

as realizations ($R = 50$) lasting 180 ms (from 60 ms before to 120 ms after the stimulus; $T = 360$ samples, $f_s = 2000$ Hz) of a vector stochastic process Y composed by $M = 10$ scalar processes, i.e. $Y_1 = E2, Y_2 = E3, Y_3 = E4, Y_4 = E5, Y_5 = E6, Y_6 = E10, Y_7 = E11, Y_8 = E12, Y_9 = E13, Y_{10} = E14$. The analysis was then performed computing the time-frequency OIR for all multiplets from order 3 to order 10 (968 multiplets). For each specimen, the OIR measures were computed after identifying the TV-VAR model (3) as described in sections 2.3, 2.4. Identification was performed on the ten time series reduced to zero mean and unit variance optimizing the model order via the MSPE procedure, setting the forgetting factor to $(1 - c) = 0.975$ [24] and the order q of the reduced models to 30 [14], and initializing the coefficient matrix ($\mathbf{A}(t_p)$) with coefficients randomly sampled from a uniform distribution in the range $[-1, 1]$.

The results are presented in figure 7 and show the time-varying (a–c) and time–frequency (d–f) OIR computed for selected multiplets of signals, along with the overall time-domain values obtained for a subset of 120 of these multiplets. Specifically, panel g shows the time-resolved OIR values averaged over the entire time window for all triplets, quadruplets, and quintuplets within each hemisphere; for two selected sextuplets — one including and one excluding the somatosensory cortices; and for all possible multiplets of order 8, 9, and 10.

The time-varying analysis shown in figures 7(a)–(c) reveals a prevalence of redundant interactions, particularly among multiplets that include signals from the contralateral hemisphere (e.g. $\Omega_{\{Y_6,Y_8,Y_{10}\}}(t_n)$, $\Omega_{\{Y_6,Y_7,Y_8,Y_{10}\}}(t_n)$, $\Omega_{\{Y_6,Y_7,Y_8,Y_9,Y_{10}\}}(t_n)$), with a marked peak occurring approximately 20 ms after stimulus onset. This pattern also holds for interactions of order nine and ten (i.e. $\Omega_{\{Y_1,\ldots,Y_9\}}(t_n)$ and $\Omega_{\{Y_1,\ldots,Y_{10}\}}(t_n)$; figure 7(c)), mirroring the trends observed in the SEP analysis shown in figure 6(b). Conversely, the time-varying OIR for signals recorded over the ipsilateral hemisphere (i.e. $\Omega_{\{Y_1,Y_3,Y_5\}}(t_n)$, $\Omega_{\{Y_1,Y_2,Y_3,Y_5\}}(t_n)$, and $\Omega_{\{Y_1,Y_2,Y_3,Y_4,Y_5\}}(t_n)$; figures 7(a) and (b)) reveals a

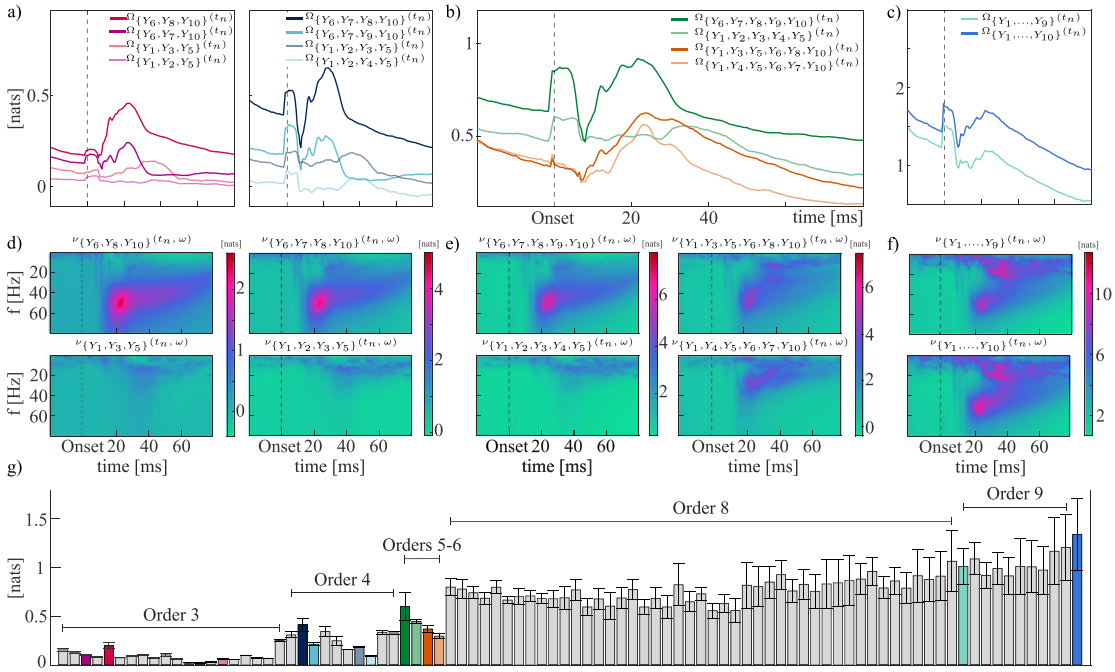

Figure 7. Time-resolved and time–frequency analysis of OIR in rats during whisker stimulation. (a)–(c) The time-varying and (d)–(f) time–frequency profiles of the OIR (median across specimens) are reported for selected multiplets (order 3 to 10). (g) Distribution (median and quartiles across specimens) of the OIR values computed for 120 selected multiplets of order 3,4,5,6,8,9 and 10 obtained integrating the time–frequency OIR over the entire frequency spectrum, and taking the average over the whole duration of the analyzed time window. The colored bar plots highlight the specific multiplets shown in panels (a)–(c).

different pattern, characterized by lower OIR values and the absence of a distinct peak. Moreover, a strong response emerges only when cS1 and iS1 are included in the same multiplet: this is evident, for example, in the analysis of sixth-order interactions (figure 7(b)), where redundancy is higher when both somatosensory areas (Y_3 and Y_8) are considered together.

These trends are confirmed by the time-frequency analysis (figures 7(d)–(f)), which also allows to localize the frequency bands where redundancy emerges. In the contralateral hemisphere (figures 7(d) and (e); first row), the clear peak of redundancy arising at $\sim$ 20 ms from the stimulation onset is localized in the gamma frequency band (40 ± 60 Hz), which is physiologically plausible as confirmed by previous studies evidencing the importance of the gamma band for the cS1 [35, 36]. A slight redundant contribution is also noticeable in the ipsilateral hemisphere (figures 7(d) and (e); second row), occurring at later latencies ($\sim$40–60 ms after the onset) and at lower frequencies, confirming the driving role of iS1 at middle latencies as suggested in [35]. This is also true when the analysis is extended to six-signal multiplets that include or exclude cS1 and iS1 (figure 7(e), second column), further confirming the key role of the contralateral and ipsilateral somatosensory cortices in the generation of HOIs. The analysis extended to nine- and ten-signal multiplets (figure 7(c)) reflects the trends observed at lower interaction orders, albeit with higher redundancy values, suggesting that high-order behaviors emerge from underlying lower-order interactions. Specifically, a rise of redundancy is noticed at $\sim$ 20 ms from the stimulus in the gamma band, and at 40-60 ms in the lower beta and alpha bands.

The analysis of the distributions across animals of the OIR displayed for 120 multiplets from order three to order ten (figure 7(g)) documents an increment of redundancy with the order of the analyzed multiplet which is coherent with previous studies analyzing overall time-domain HOIs with time-invariant approaches [12, 14]. The patterns of HOIs confirm the presence of net redundancy in all the analyzed multiplets, and identify key multiplets depending on the analyzed order of interactions. Specifically, for interaction orders three to five, the inclusion of processes Y_6, Y_8, and Y_{10} in the analyzed multiplets results in higher redundancy values compared to their ipsilateral counterparts Y_1, Y_3, and Y_5. The highest redundancy values are detected in the multiplets of order six only when cS1 and iS1 are considered together. It is worth of note that, when the analyzed multiplet comprises the majority of the electrodes belonging to the contralateral hemisphere, the redundancy is higher. These findings highlight the dominant role of the contralateral sensory cortex (electrodes E10, E12, E14) in mediating redundant interactions.

Overall, the redundancy-dominated networks observed in both the contralateral and ipsilateral hemispheres can be explained in terms of several previous findings [35, 36, 55, 56] and considering the

results from the simulation study performed herein. Specifically, whisker-evoked activity originates in cS1 (process Y_8, electrode $E12$), with significant functional outflow occurring at early latencies [56]. The functional connections from cS1 preferentially target frontal sensorimotor and parietal regions ($Y_6 = E10$ and $Y_{10} = E14$ in figure 6), consistently with the strong structural connectivity between cS1 and these regions [55]. These findings also align with the sequential activation patterns observed in the analysis of SEPs (figure 6) [35, 36], as well as prior work showing a high degree of causal connectivity among the signals recorded from contralateral electrodes [35, 36]. Furthermore, our simulation study supports the presence of redundancy originating from a common driver structure, where cS1 influences the dynamics of multiple targets. The time–frequency analysis of OIR further confirms that this interaction is primarily redundant, supporting the hypothesis that redundancy in brain networks enables overlapping information storage across regions, thereby contributing to the stability and resilience of cognitive and motor functions. These findings reinforce the central role of cS1 in coordinating activity across frontal and parietal areas and highlight the importance of the contralateral hemisphere in sustaining HOIs in this setting.

5. Conclusions

The novel methodology presented in this work significantly advances the set of tools for the study of high-order interdependencies in dynamic network systems. Indeed, while being solidly grounded in frameworks recently introduced to characterize synergy- and redundancy-dominated circuits in networks of random variables [20] and random processes [7], it significantly expands the applicability of these frameworks providing time-varying and time-frequency measures of HOIs. This peculiarity enables the analysis of non-stationary and frequency-specific behaviors which are very common in computational neuroscience and physiology.

We demonstrated that the time-resolved and time-frequency analyzes are tightly interconnected through the spectral integration property of information-theoretic measures, enabling a consistent derivation of time-varying measures from the expanded time-frequency metric. Our framework allows for the straightforward computation of measures representing HOIs at any order, starting from the identification of time-varying linear models using a RLS estimator with a forgetting factor, which ensures a reliable estimation of both slow transitions and fast intermittent behaviors. Moreover, the strategy introduced in this work allows for the time-resolved computation of prediction error variances for restricted models, laying the groundwork for a future causal decomposition of the OIR into components reflecting Granger-causal and instantaneous influences, which could be estimated in both the time and time-frequency domains [7]. The extension to multi-trial settings, also introduced here, allows for robust model identification across repeated realizations, which is crucial for applications such as brain evoked responses where non-stationarities are expected and well documented.

The theoretical example and the applications to physiological and brain networks showcase the potential of extending information-theoretic measures to capture the balance between redundancy and synergy among large groups of nodes, even in the presence of significant non-stationarities. Moreover, our approach underscores the importance of analyzing interactions in the time-frequency domain, enabling the detection of frequency-specific interactions that may remain hidden in time-domain and even time-varying analyzes. The data-driven nature of the proposed method makes it applicable not only to biomedical time series but also to a wide range of dynamic systems, including electronic, climatological, social, and financial networks, where the activity of each node can be modeled and studied using the theory of stochastic processes.

Data availability statement

The data support the findings of this study are openly available at the followiing URL: https://github.com/YuriAntonacci/tv-OIR-toolbox.

The epicranial EEG data are part of previous works [35, 36], and can be found here: https://doi.org/10.6084/m9.figshare.5909122.v1

Acknowledgments

The authors would like to gratefully thank Prof. Michal Javorka for sharing part of the data used in this work.

Y A and L F were partially supported by SiciliAn MicronanOTecH Research And Innovation CEnter 'SAMOTHRACE' (MUR, PNRR-M4C2, ECS_00000022), spoke 3 - Universitá degli Studi di Palermo 'S2-COMMs—Micro and Nanotechnologies for Smart & Sustainable Communities. L F was partially supported by PRIN 2022 Project 'HONEST-High-Order Dynamical Networks in Computational Neuroscience and Physiology: an Information-Theoretic Framework' (funded by MUR, code 2022YMHNPY, CUP B53D23003020006). L M gratefully acknowledges the support of the 'Hundred Talents' program of the University of Electronic Science and Technology of China, of the 'Outstanding Young Talents Program (Overseas)' program of the National Natural Science Foundation of China, and of the talent programs of the Sichuan province and Chengdu municipality.

ORCID iDs

Yuri Antonacci 0000-0002-6956-6323
Chiara Bará 0000-0002-1307-8662
Laura Sparacino 0000-0001-8969-9257
Gorana Mijatovic 0000-0002-7409-8130
Ludovico Minati 0000-0002-2532-1674
Luca Faes 0000-0002-3271-5348

References

[1] Santoro A, Battiston F, Lucas M, Petri G and Amico E 2024 Higher-order connectomics of human brain function reveals local topological signatures of task decoding, individual identification and behavior *Nat. Commun.* **15** 10244
[2] Rubinov M and Sporns O 2010 Complex network measures of brain connectivity: uses and interpretations *Neuroimage* **52** 1059–69
[3] Lehnertz K, Bröhl T and Rings T 2020 The human organism as an integrated interaction network: recent conceptual and methodological challenges *Front. Physiol.* **11** 598694
[4] Battiston F, Cencetti G, Iacopini I, Latora V, Lucas M, Patania A, Young J-G and Petri G 2020 Networks beyond pairwise interactions: structure and dynamics *Phys. Rep.* **874** 1–92
[5] Antonacci Y, Minati L, Nuzzi D, Mijatovic G, Pernice R, Marinazzo D, Stramaglia S and Faes L 2021 Measuring high-order interactions in rhythmic processes through multivariate spectral information decomposition *IEEE Access* **9** 149486–505
[6] Varley T F 2024 A synergistic perspective on multivariate computation and causality in complex systems *Entropy* **26** 883
[7] Faes L, Mijatovic G, Antonacci Y, Pernice R, Barà C, Sparacino L, Sammartino M, Porta A, Marinazzo D and Stramaglia S 2022 A new framework for the time-and frequency-domain assessment of high-order interactions in networks of random processes *IEEE Trans. Signal Process.* **70** 5766–77
[8] Sparacino L, Antonacci Y, Mijatovic G and Faes L 2025 Measuring hierarchically-organized interactions in dynamic networks through spectral entropy rates: theory, estimation and illustrative application to physiological networks *Neurocomputing* **630** 129675
[9] Mijatovic G, Sparacino L, Antonacci Y, Javorka M, Marinazzo D, Stramaglia S and Faes L 2024 Assessing high-order links in cardiovascular and respiratory networks via static and dynamic information measures *IEEE Open J. Eng. Med. Biol.* **5** 846–58
[10] Mijatovic G, Antonacci Y, Javorka M, Marinazzo D, Stramaglia S and Faes L 2025 Network representation of higher-order interactions based on information dynamics *IEEE Trans. Netw. Sci. Eng.* **12** 1872–84
[11] Luppi A I, Rosas F E, Mediano P A M, Demertzi A, Menon D K and Stamatakis E A 2024 Unravelling consciousness and brain function through the lens of time, space and information *Trends Neurosci.* **47** 551–68
[12] Antonacci Y, Barà C, Sparacino L, Pirovano I, Mastropietro A, Rizzo G and Faes L 2024 Spectral information dynamics of cortical signals uncover the hierarchical organization of the human brain's motor network *IEEE Trans. Biomed. Eng.* **75** 1655–64
[13] Pirovano I, Antonacci Y, Mastropietro A, Bara C, Sparacino L, Guanziroli E, Molteni F, Tettamanti M, Faes L and Rizzo G 2023 Rehabilitation modulates high-order interactions among large-scale brain networks in subacute stroke *IEEE Trans. Neural Syst. Rehabil. Eng.* **31** 4549–60
[14] Sparacino L, Faes L, Mijatović G, Parla G, Re V L, Miraglia R, de Ville de Goyet J and Sparacia G 2023 Statistical approaches to identify pairwise and high-order brain functional connectivity signatures on a single-subject basis *Life* **13** 2075
[15] Varley T F, Pope M, Faskowitz J and Sporns O 2023 Multivariate information theory uncovers synergistic subsystems of the human cerebral cortex *Commun. Biol.* **6** 451
[16] Varley T F, Pope M, Grazia M, Joshua F and Sporns O 2023 Partial entropy decomposition reveals higher-order information structures in human brain activity *Proc. Natl Acad. Sci.* **120** e2300888120
[17] Williams P L and Beer R D 2010 Nonnegative decomposition of multivariate information (arXiv:1004.2515)
[18] Stramaglia S, Scagliarini T, Daniels B C and Marinazzo D 2021 Quantifying dynamical high-order interdependencies from the o-information: an application to neural spiking dynamics *Front. Physiol.* **11** 595736
[19] Stramaglia S, Faes L, Cortes J M and Marinazzo D 2024 Disentangling high-order effects in the transfer entropy *Phys. Rev. Res.* **6** L032007
[20] Rosas F E, Mediano P A, Gastpar M and Jensen H J 2019 Quantifying high-order interdependencies via multivariate extensions of the mutual information *Phys. Rev. E* **100** 032305
[21] McGill W 1954 Multivariate information transmission *Trans. IRE Prof. Group Inf. Theory* **4** 93–111
[22] Hesse W, Möller E, Arnold M and Schack B 2003 The use of time-variant EEG granger causality for inspecting directed interdependencies of neural assemblies *J. Neurosci. Methods* **124** 27–44
[23] Ivanov P C 2021 The new field of network physiology: building the human physiolome *Front. Netw. Physiol.* **1** 711778
[24] Antonacci Y, Barà C, Zaccaro A, Ferri F, Pernice R and Faes L 2023 Time-varying information measures: an adaptive estimation of information storage with application to brain-heart interactions *Front. Netw. Physiol.* **3** 1242505
[25] Antonacci Y, Barà C, de Felice G, Sferlazza A, Pernice R and Faes L 2025 Exploring transient neurophysiological states through local and time-varying measures of information dynamics *Appl. Math. Comput.* **500** 129437
[26] Ivanov P C, Amaral L N, Goldberger A L and Stanley H E 1998 Stochastic feedback and the regulation of biological rhythms *Europhys. Lett.* **43** 363
[27] Scagliarini T, Marinazzo D, Guo Y, Stramaglia S and Rosas F E 2022 Quantifying high-order interdependencies on individual patterns via the local o-information: Theory and applications to music analysis *Phys. Rev. Res.* **4** 013184
[28] Pope M, Varley T F, Puxeddu M G, Faskowitz J and Sporns O 2025 Time-varying synergy/redundancy dominance in the human cerebral cortex *J. Phys. Complex.* **6** 015015
[29] Haykin S 2002 Adaptive filter theory *Prentice Hall Google Schola* vol 2 pp 67–94
[30] Möller E, Schack B, Arnold M and Witte H 2001 Instantaneous multivariate EEG coherence analysis by means of adaptive high-dimensional autoregressive models *J. Neurosci. Methods* **105** 143–58
[31] Möller E, Schack B, Vath N and Witte H 2003 Fitting of one arma model to multiple trials increases the time resolution of instantaneous coherence *Biol. Cybern.* **89** 303–12
[32] Milde T, Leistritz L, Astolfi L, Miltner W H, Weiss T, Babiloni F and Witte H 2010 A new kalman filter approach for the estimation of high-dimensional time-variant multivariate ar models and its application in analysis of laser-evoked brain potentials *Neuroimage* **50** 960–9
[33] Astolfi L *et al* 2008 Tracking the time-varying cortical connectivity patterns by adaptive multivariate estimators *IEEE Trans. Biomed. Eng.* **55** 902–13
[34] Cerutti S, Mainardi L T and Bianchi A M 2002 Time-frequency and time-varying analysis for assessing the dynamic responses of cardiovascular control *Crit. Rev.™ Biomed. Eng.* **30** 1–3
[35] Plomp G, Quairiaux C, Michel C M and Astolfi L 2014 The physiological plausibility of time-varying granger-causal

modeling: normalization and weighting by spectral power *NeuroImage* **97** 206–16
[36] Pagnotta M F and Plomp G 2018 Time-varying mvar algorithms for directed connectivity analysis: critical comparison in simulations and benchmark eeg data *PLoS One* **13** e0198846
[37] Barbieri R, Frank L M, Nguyen D P, Quirk M C, Solo V, Wilson M A and Brown E N 2004 Dynamic analyses of information encoding in neural ensembles *Neural Comput.* **16** 277–307
[38] Cover T M 1999 *Elements of Information Theory* (Wiley)
[39] Faes L, Porta A, Nollo G and Javorka M 2016 Information decomposition in multivariate systems: definitions, implementation and application to cardiovascular networks *Entropy* **19** 5
[40] Faes L, Stramaglia S and Marinazzo D 2017 On the interpretability and computational reliability of frequency-domain granger causality *F1000Research* vol 6 (https://doi.org/10.12688/f1000research.12694.1)
[41] Barnett L and Seth A K 2014 The MVGC multivariate granger causality toolbox: a new approach to granger-causal inference *J. Neurosci. Methods* **223** 50–68
[42] Faes L, Erla S and Nollo G 2012 Measuring connectivity in linear multivariate processes: definitions, interpretation and practical analysis *Comput. Math. Methods Med.* **2012** 1–18
[43] Robert T and Mialhes C 1996 Continuously evolving classification using time-varying ar modeling *Proc. Third Int. Symp. on Time-Frequency and Time-Scale Analysis (TFTS-96)* (IEEE) pp 241–4
[44] Hodgkiss W and Presley J 1981 Adaptive tracking of multiple sinusoids whose power levels are widely separated *IEEE Trans. Circuits Syst.* **28** 550–61
[45] Chicharro D 2011 On the spectral formulation of granger causality *Biol. Cybern.* **105** 331–47
[46] Grieszbach G, Schack B, Putsche P, Bareshova E and Bolten J 1994 Dynamic description of stochastic signal by adaptive momentary power and momentary frequency estimation and its application in analysis of biological signals *Med. Biol. Eng. Comput.* **32** 632–7
[47] Costa A H and Hengstler S 2011 Adaptive time–frequency analysis based on autoregressive modeling *Signal Process.* **91** 740–9
[48] Lütkepohl H 2005 *New Introduction to Multiple Time Series Analysis* (Springer)
[49] Antonacci Y, Toppi J, Pietrabissa A, Anzolin A and Astolfi L 2024 Measuring connectivity in linear multivariate processes with penalized regression techniques *IEEE Access* **12** 30638–52
[50] Antonacci Y, Astolfi L, Nollo G and Faes L 2020 Information transfer in linear multivariate processes assessed through penalized regression techniques: validation and application to physiological networks *Entropy* **22** 732
[51] Iovino M, Lazic I, Loncar-Turukalo T, Javorka M, Pernice R and Faes L 2024 Comparison of automatic and physiologically-based feature selection methods for classifying physiological stress using heart rate and pulse rate variability indices *Physiol. Meas.* **45** 115004
[52] Faes L, Pernice R, Mijatovic G, Antonacci Y, Krohova J C, Javorka M and Porta A 2021 Information decomposition in the frequency domain: a new framework to study cardiovascular and cardiorespiratory oscillations *Phil. Trans. R. Soc. A* **379** 20200250
[53] Barà C, Sparacino L, Pernice R, Antonacci Y, Porta A, Kugiumtzis D and Faes L 2023 Comparison of discretization strategies for the model-free information-theoretic assessment of short-term physiological interactions *Chaos* **33** 033127
[54] Porta A, Bari V, De Maria B, Takahashi A C, Guzzetti S, Colombo R, Catai A M, Raimondi F and Faes L 2017 Quantifying net synergy/redundancy of spontaneous variability regulation via predictability and transfer entropy decomposition frameworks *IEEE Trans. Biomed. Eng.* **64** 2628–38
[55] Quairiaux C, Sizonenko S V, Mégevand P, Michel C M and Kiss J Z 2010 Functional deficit and recovery of developing sensorimotor networks following neonatal hypoxic–ischemic injury in the rat *Cereb. Cortex* **20** 2080–91
[56] Quairiaux C, Mégevand P, Kiss J Z and Michel C M 2011 Functional development of large-scale sensorimotor cortical networks in the brain *J. Neurosci.* **31** 9574–84
[57] Javorka M, Krohova J, Czippelova B, Turianikova Z, Lazarova Z, Javorka K and Faes L 2017 Basic cardiovascular variability signals: mutual directed interactions explored in the information domain *Physiol. Meas.* **38** 877
[58] Krohova J, Faes L, Czippelova B, Pernice R, Turianikova Z, Wiszt R, Mazgutova N, Busacca A and Javorka M 2020 Vascular resistance arm of the baroreflex: methodology and comparison with the cardiac chronotropic arm *J. Appl. Physiol.* **128** 1310–20
[59] Javorka M, Dávid Š, Bikia V, Czippelová B, Stergiopulos N and Krohová J Č 2024 In silico validation of non-invasive arterial compliance estimation and potential determinants of its variability *Physiol. Res.* **73** S771
[60] Porta A, Catai A M, Takahashi A C, Magagnin V, Bassani T, Tobaldini E, De Borne P V and Montano N 2011 Causal relationships between heart period and systolic arterial pressure during graded head-up tilt *Am. J. Physiol. Regul. Integr. Comp. Physiol.* **300** R378–86
[61] Cohen M A and Taylor J A 2002 Short-term cardiovascular oscillations in man: measuring and modelling the physiologies *J. Physiol.* **542** 669–83
[62] Vybiral T, Bryg R J, Maddens M E and Boden W E 1989 Effect of passive tilt on sympathetic and parasympathetic components of heart rate variability in normal subjects *Am. J. Cardiol.* **63** 1117–20
[63] Javorka M, Krohova J, Czippelova B, Turianikova Z, Lazarova Z, Wiszt R and Faes L 2018 Towards understanding the complexity of cardiovascular oscillations: Insights from information theory *Comput. Biol. Med.* **98** 48–57
[64] Faes L, Nollo G and Porta A 2013 Mechanisms of causal interaction between short-term rr interval and systolic arterial pressure oscillations during orthostatic challenge *J. Appl. Physiol.* **114** 1657–67
[65] Krohova J, Faes L, Czippelova B, Turianikova Z, Mazgutova N, Pernice R, Busacca A, Marinazzo D, Stramaglia S and Javorka M 2019 Multiscale information decomposition dissects control mechanisms of heart rate variability at rest and during physiological stress *Entropy* **21** 526
[66] Wiest M C, Bentley N and Nicolelis M A 2005 Heterogeneous integration of bilateral whisker signals by neurons in primary somatosensory cortex of awake rats *J. Neurophysiol.* **93** 2966–73